J. Geomag. Geoelectr., **45**, 1115–1126, 1993

Electrical Anisotropy in the Lower Crust of British Columbia: an Interpretation of a Magnetotelluric Profile after Tensor Decomposition

Markus EISEL[1] and Karsten BAHR[2]

[1] *GeoForschungsZentrum Potsdam, Telegrafenberg A45, 14473 Potsdam, Germany*
[2] *Institut fuer Meteorologie und Geophysik, Feldbergstr. 47, 60054 Frankfurt, Germany*

(Received February 25, 1993; Revised August 4, 1993; Accepted September 2, 1993)

The application of a magnetotelluric (MT) tensor decomposition scheme to the long period responses of the BC87 data set yields an almost two-dimensional regional conductivity structure with a strike of N45°E. The main feature in the MT responses of the observed region are diverging apparent resistivity curves and phase differences.

1-D modelling and 2-D inversion of different combinations of these MT parameters suggest the existence of a strongly anisotropic layer in the middle to lower crust. Based on the 1-D estimates for resistivities, and using the geometry from the 2-D inversion, a 2-D forward model is derived which includes a strongly anisotropic layer at 30 km depth with the two principal resistivities of 300 Ωm and 5 Ωm. This model explains mainly the phases of the impedance tensor at longer periods. The apparent resistivities are affected by small-scale, near surface inhomogeneities.

1. Introduction

The first Magnetotelluric Data Interpretation Workshop (MT-DIW1) preceded the 11th Workshop on Electromagnetic Induction in the Earth in Wellington, New Zealand. The purpose of this workshop was to compare and discuss the results of different interpretation schemes applied to two different datasets. This paper deals with the interpretation of the second dataset, BC87. The magnetotelluric responses were obtained along an east-west profile in south-eastern British Columbia as part of the LITHOPROBE Southern Cordillerean Transect investigation (JONES *et al.*, 1988; JONES, 1993). MT tensor impedances for 27 sites in a frequency range from 500 Hz to 0.0005 Hz provide the basis for the interpretation.

BAHR's (1991) decomposition scheme was applied to these data to obtain the strike of the regional 2-D structure and two principal phases. It is described in Section 2. Using the results from the decomposition, one-dimensional modelling of anisotropic structures and two-dimensional inversions for smooth models (DEGROOT-HEDLIN and CONSTABLE, 1990) yielded the basic parameters for final two-dimensional forward modelling. This is described in Section 3.

2. Phase Distortion Correction and Discussion of the Dimensionality

Techniques for the decomposition of the magnetotelluric impedance tensor into parameters relevant to a general Earth model that allows for 3-D galvanic distortion and regional 2-D induction have recently been reviewed by GROOM and BAHR (1992). By use of these techniques the complex 2×2 magnetotelluric impedance matrix is decomposed into eight real parameters: the strike of the regional conductivity structure, the two principal apparent resistivities, the two principal phases, two decomposition parameters that describe only the effect of galvanic distortion and a residual that describes departures of the regional structure from pure two-dimensionality. BAHR (1988) suggested a "regional" or "phase-sensitive" skew in order to provide a measure of the dimensionality of the regional structure. GROOM and BAILEY (1989) introduced an "error

of fit" of an inverse technique by which the decomposition parameters are extracted from the data. The regional skew and the "error of fit" can be considered as alternative realizations of the eighth decomposition parameter which describes possible departures from two-dimensionality. The general decomposition problem is underestimated because the two principal apparent resistivities may still be affected by static shifts (BAHR, 1991; GROOM and BAHR, 1992). Therefore

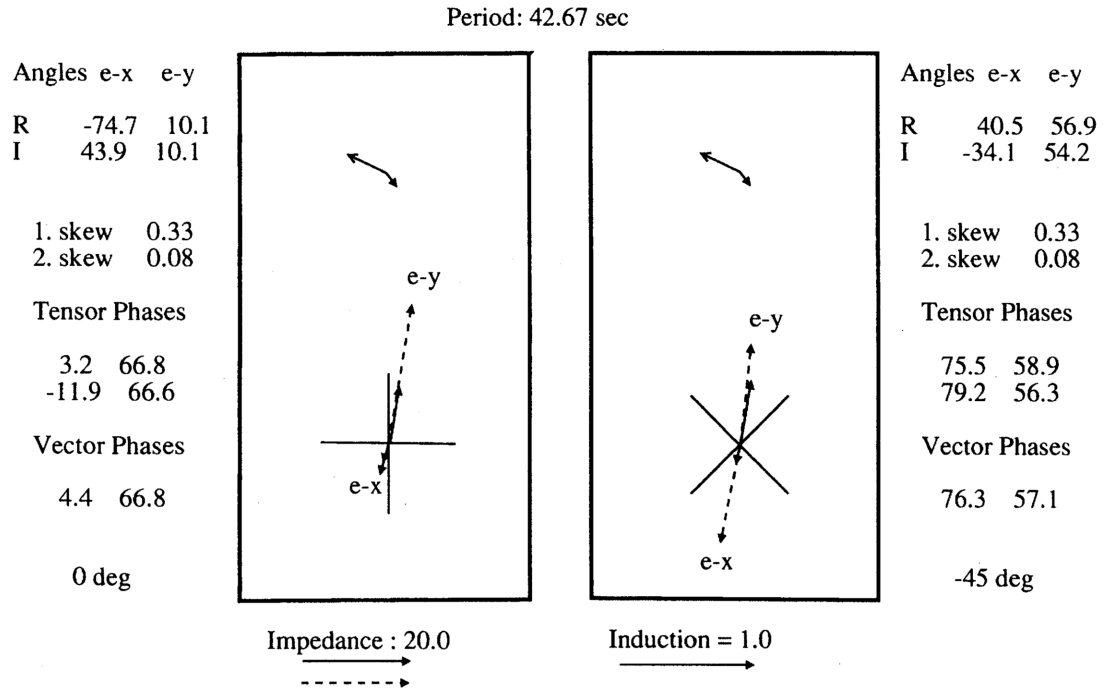

Fig. 1. Decomposition parameters of site *s*001 for the period 42 s. Left: In the coordinate frame of the measurement. Right: rotated by 45°. Displayed are the skew angles separately for the real and the quadrature part of the impedance. In the middle, the telluric vectors are plotted. The dashed lines refer to the quadrature part. The phases of the four elements of the impedance tensor are shown along with the phases of the telluric vectors. Note that after rotation these phases satisfy the decomposition condition, and the real and the quadrature part of each telluric vector have similar skew angles.

the most important decomposition parameters that can be interpreted with conductivity models are the regional strike direction and the regional phases. If data from a profile are interpreted, these decomposition parameters should vary smoothly from site to site.

Small-scale conductivity anomalies can cause both static shifts and phase mixing of the two regional phases of a regional 2-D structure (GROOM and BAHR, 1992). Only the second effect is considered here. We apply BAHR's (1991) modified decomposition technique to the BC87 dataset in an attempt to check whether the assumption of regional two-dimensionality that underlies the decomposition techniques is fulfilled.

2.1 Determination of distortion classes and regional strike

The regional strike is the decomposition parameter which is most difficult to find (GROOM and BAHR, 1992; JONES and GROOM, 1993). For some of the BC87 data it cannot be obtained

from MT responses alone. Figure 1 shows the "telluric vectors" of site $s001$ for the period 42 s. Let $\hat{x}, \hat{y}$ be unit vectors in the north and east directions, respectively. The two columns of the impedance tensor are presented in terms of two complex "telluric vectors":

$$\vec{e_x} = Z_{xx}\hat{x} + Z_{yx}\hat{y}, \tag{1a}$$

$$\vec{e_y} = Z_{xy}\hat{x} + Z_{yy}\hat{y}. \tag{1b}$$

These two vectors are antiparallel for site $s001$, regardless of whether they are calculated in geomagnetic coordinates (Fig. 1, left) or in a coordinate system rotated N45°E (Fig. 1, right). Thus, this site represents the "class 6" type of distortion (BAHR, 1991, p. 33). However, if rotated, the phases of the tensor elements fulfill the decomposition condition that Z_{xx} and Z_{yx} have equal phases and Z_{yx} and Z_{yy} also have equal phases (Fig. 1, right).

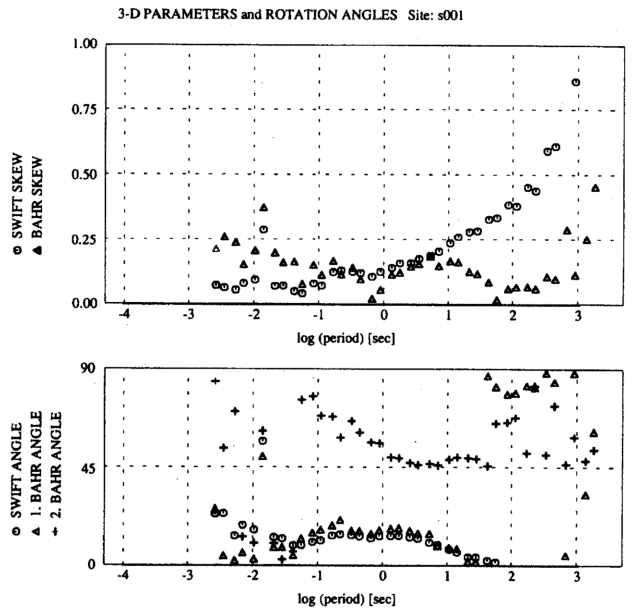

Fig. 2. Decomposition parameters "skew" and "angle" as a function of period for site $s001$. For further explanation, see text.

This situation occurs frequently in the BC87 data. Table 2 in the appendix provides a summary of distortion classes and regional strike angle determinations for all sites at selected long periods. For a detailed description of the distortion classes the reader is referred to BAHR (1991). The decomposition will fail to produce a reliable regional strike in the case of distortion class 6 where severe local channeling occurs, but it will also fail in the case of class 7 where the regional skew is too large; this case is discussed in the next section. For those sites which belong to these two classes a strike is suggested that results in phases similar to those of neighbouring sites. For class 2 sites a strike angle determination is not possible because the phase differences between MT tensor elements are small. This applies only to site $s014$. We have no explanation for this effect as site $s014$ is situated very close to site $s015$ and should therefore show similar regional decomposition parameters. In class 5 the general superposition model holds and most confidence should be given to the regional strike estimated from "class 5" sites. The symbols 5/6

and 5/7 describe datasets that are "almost" in class 6 or 7, but a rough estimate of the regional strike can nevertheless be calculated by use of the modified superposition model in which the impedance matrix takes the form

$$Z = \begin{pmatrix} -a_{12} Z_{nyx} e^{i\delta} & a_{11} Z_{nxy} \\ -a_{22} Z_{nyx} & a_{21} Z_{nxy} e^{-i\delta} \end{pmatrix} \tag{2}$$

in the coordinate frame of the regional strike (BAHR, 1991, Eq. 22). The parameter δ can be considered as another display of departures from the model of ideal regional 2-dimensionality beside fit error and regional skew. From Table 2 an average regional strike of 45° can be found for 12 sites ($s006$, $s008$–$s013$, $s015$–$s019$) in the middle of the profile. However, the strike angles of individual sites show some scatter, probably due to the fact that the condition of regional two-dimensionality is not fulfilled entirely, as indicated by non-zero δ values in Table 2.

2.2 Departures from regional two-dimensionality

"1. skew" and "2. skew" in Fig. 1 refer to conventional and phase-sensitive skew (Eq. 5 and Eq. 12 in BAHR, 1991, respectively) of site $s001$. They are displayed in Fig. 2 (top) for the entire period range. Figures 3 and 4 display the conventional skew and the phase-sensitive skew for all sites and frequencies from 1.1 Hz to 0.002 Hz. While the conventional skew becomes very large at long periods (indicating 3-D distortion due to local anomalies), the phase-sensitive skew is smaller.

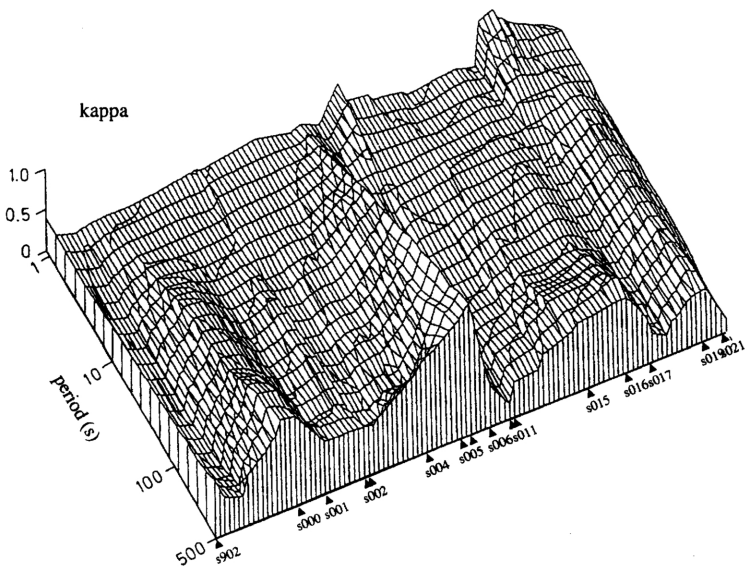

Fig. 3. Decomposition parameters "conventional skew" (kappa) as a function of frequency and location. Triangles point to the site locations on an east-west striking profile on which the BC87 sites have been projected. The conventional skew "kappa" shows very high values in the whole frequency range and over the whole profile with rough changes from one site to another. Its maxima exceed 0.8 at sites $s000$, $s005$, $s016$ for periods larger than 100 sec.

This phase-sensitive skew is nevertheless in the range of 0.1–0.2, and therefore still large compared to the relative error bars of the impedance matrix elements. It should be mentioned that in the period range 1 s–100 s the data quality is excellent (errors $\approx$ 1%). TING and HOHMANN

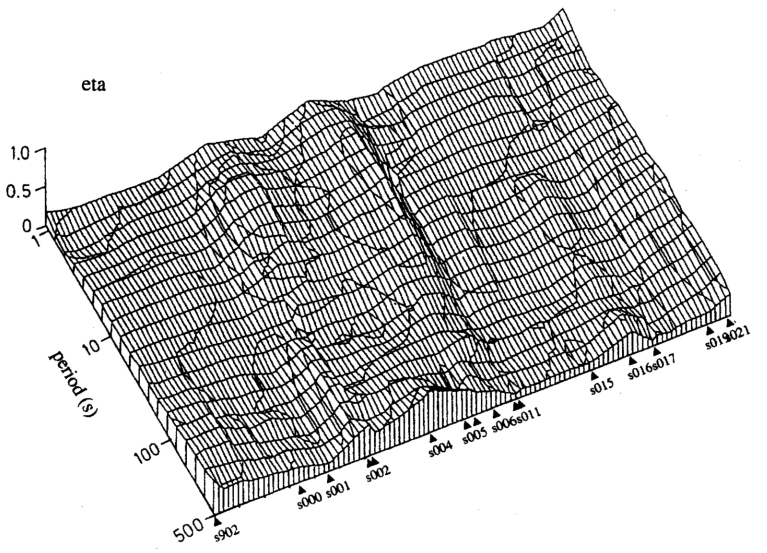

Fig. 4. Decomposition parameters "phase-sensitive skew" (eta) as a function of frequency and location. In opposition to the "conventional skew" (Fig. 3) "eta"-values are below 0.3 everywhere and have minima smaller than 0.1 between sites *s*011 and *s*015.

(1981) calculated the conventional skew for the special 3-D conductivity model of a rectangular anomaly. Because they did not include surface anomalies in their model, this skew describes the regional dimensionality of the model impedance. It should therefore be compared with the regional skew calculated from the field data. TING and HOHMANN (1981) obtained maximal skew values of 0.15 that are comparable to the regional skew values which we obtained from some of the BC87 sites. Only the data of sites *s*009, *s*010, *s*015 and *s*017 yielded regional skew values below 0.1 (this is also indicated by the small δ values of these sites in Table 2). Seven sites yielded regional skew values in the range 0.2–0.3 (distortion class 5/7), and three sites cannot be described by two-dimensional regional structures at all (distortion class 7). Even if these "class 7" sites are considered as exceptions, it must be concluded from the comparison of the field data skew with the model results of TING and HOHMANN (1981) that some regional 3D structures affect most of the sites of the BC87 dataset.

It should also be noted that sites with small regional skew show a local maximum of this parameter at 5 s period. Figure 2 shows this for site *s*001 as an example. The maximum divides long periods with a regional strike of 45° from shorter periods with regional strike of 60° (JONES and GROOM, 1993). Calculating the penetration depth from resistivities of the final model and 5 sec period gives 30 km. This could indicate that the origin of the weak regional three-dimensionality is situated at this depth.

However, the strike angles and two regional phases obtained from the decomposition are consistent from site to site. This provides evidence that most of the observed phase splitting is due to a major 2-D structure with principal directions parallel and perpendicular to N45°E. The geometry of this structure is investigated in the following section.

3. Modelling Process

As it is not possible to estimate the static shift factors, the purpose of the modelling procedure is to fit the two regional phases of the tensors. Figure 5 shows one example of the data before and after rotation. In unrotated coordinates the phase of the tensor element Z_{yx} is larger than 90°, which cannot be interpreted by 1-D or 2-D models. After rotation both phases are within the range of 0° to 90°. In the rotated coordinate frame, and for periods longer than a few seconds, the phases of the tensor elements Z_{yx} are remarkably smaller than those of elements Z_{xy}. This applies to almost all sites after rotation into the N45°E coordinate system. The fact that the apparent resistivities are not consistent with this behavior, i.e. the values of Z_{yx} are smaller than those of Z_{xy}, is due to strong distortion effects but does not apply to all sites. Conventionally regional 2-D structures are assumed to be responsible for the observed features. Such a structure would result in a regional anomaly of the vertical magnetic field at least at some periods. But the observed vertical magnetic field in the target area is small. An alternative explanation might be a laterally anisotropic structure in the 30 km depth range. This corresponds to the penetration depths of periods longer than 5 s–10 s where the phase splitting starts.

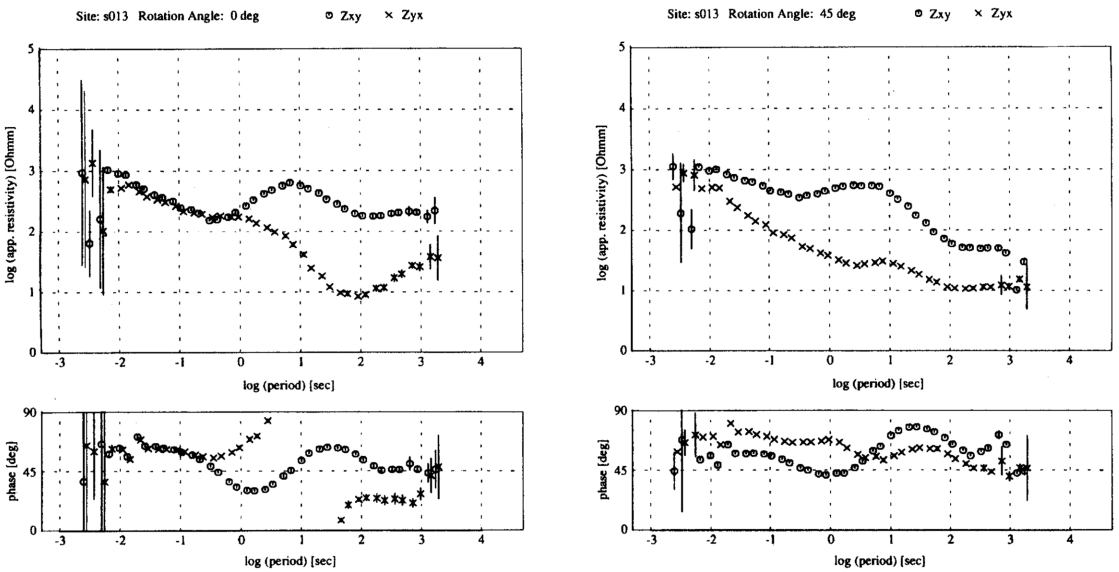

Fig. 5. Apparent resistivity and phase curves for the site *s*013 in unrotated coordinates (left) and rotated about 45° (right). In the rotated coordinate frame the phases are in the defined range of 0° to 90°, whereas in the unrotated coordinates they are not. For periods longer than a few seconds the phase of Z_{xy} is significantly higher than that of Z_{yx} for all the sites.

This anisotropic structure can be identified with the regional 2-D conductivity anomaly on which the decomposition model is based. The two principal phases emerge from the anisotropy. Consider a working model in which vertical lamellae of two different resistivities result in a lateral electrical anisotropy with major and minor resistivity perpendicular and parallel to the lamellae. If these lamellae have macroscopic extension their orientation defines a strike angle of the resulting 2-D structure. Two principal MT responses can be calculated for this model. The direction of lower resistivity can be identified with the TE mode, and the direction of higher resistivity with the TM mode.

3.1 2-D inversion

The OCCAM2 inversion program (DEGROOT-HEDLIN and CONSTABLE, 1990) was used to generate two-dimensional models. Data at six frequencies between 18 Hz and 0.017 Hz from 11 almost equally spaced sites were used for the inversion. Inversions were carried out for the following combinations of MT parameters:

- $\varrho_{a,TE}$ and φ_{TE}
- $\varrho_{a,TM}$ and φ_{TM}
- $\varrho_{a,TE}$ and φ_{TE} and φ_{TM}
- $\varrho_{a,TM}$ and φ_{TM} and φ_{TE}
- φ_{TE}
- φ_{TM}
- φ_{TM} and φ_{TE}.

$\varrho_{a,TE}$, $\varrho_{a,TM}$ refer to the principal apparent resistivities and φ_{TE}, φ_{TM} to the principal phases in the N45°E coordinate frame.

The models are not shown here for reasons of space but the results are described briefly. Inverting only the phases of the two modes together resulted in the smoothest model. Its geometry is very similar to those models from separate inversion of the individual phases. Including the apparent resistivities yielded extremely high model resistivities.

Comparing the results from inverting the phases of the TE and TM mode separately shows that the model for the TE mode has higher conductivities at depths greater than 30 km underlying more resistive material, and vice-versa for the TM mode model: here the resistivities are relatively small in the upper part of the model and increase with depth. But in both models the transition is approximately at the same depth. The joint inversion of both phases also shows a significant change in resistivity structure at about 30 km depth. There is no change in this result if the TM mode apparent resistivities are included. The absolute resistivities of these models have not very much relevance and they should only be regarded as relative values.

Nevertheless the two models from separate inversion of TE phases and TM phases also point to the existence of an anisotropic layer as mentioned above. A model including an anisotropic layer will fulfill the required transition to higher resistivities for the one polarization and to lower resistivities for the other polarization at the same depth.

3.2 1-D anisotropic modelling

An algorithm of DEKKER and HASTIE (1980) was used for forward calculations of one-dimensional anisotropic layered models. The model consists of a number of layers with two resistivities in perpendicular horizontal directions within the layers. Within each layer the direction of the minor and major resistivity is arbitrary. Figure 6 shows the apparent resistivity and phase curves of site *s*019 in unrotated (left) and rotated (45°) coordinates (right) together with the curves of a 1-D anisotropic model in the same coordinate frames. The model parameters are given in Table 1. The yx-elements of the model are shifted by a factor of 3.

Table 1. The parameters of the one-dimensional anisotropic model for site *s*019. The two resistivities within each layer are minor and major horizontal resistivities, the angle ϕ is the deviation of their direction from a north-east coordinate frame (see Fig. 6).

layer	ϱ_1[Ωm]	ϱ_2[Ωm]	thickness [km]	ϕ[deg]
1	800	800	15	0
2	5	300	20	45
3	200	200	5	0
4	1000	1000	∞	0

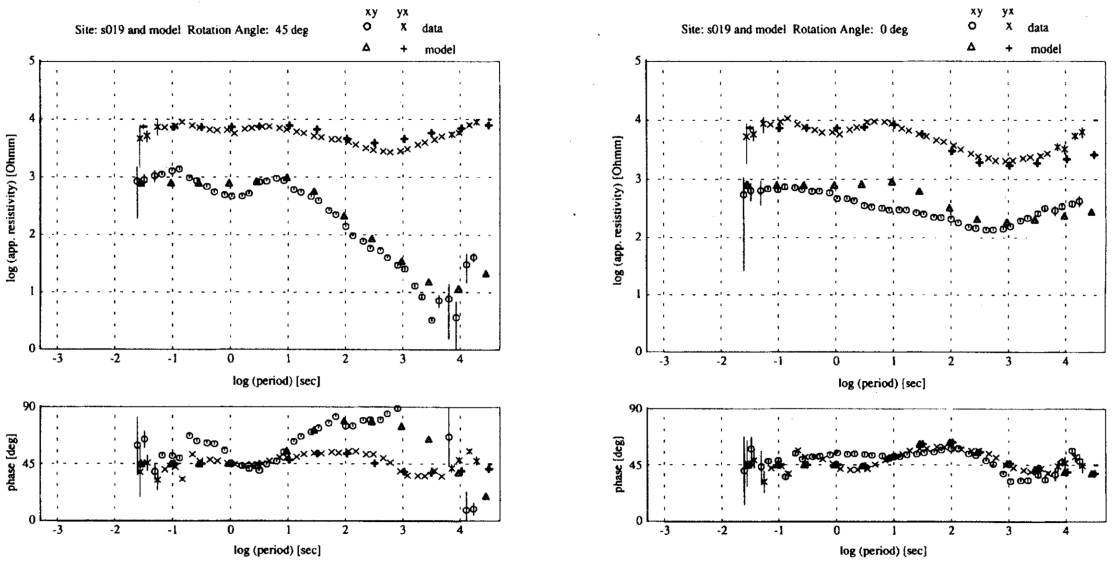

Fig. 6. Apparent resistivity and phase curves for site *s*019 and the 1-D anisotropic model displayed in Table 1 in unrotated and rotated coordinate frames. The yx-element of the model tensors is shifted by a factor of 3. The dense spaced symbols (circles and $\times$) are the field data, the wider spaced triangles and $+$ are the model data. The model phases of the two tensor elements in unrotated coordinates are equal as the apparent resistivity values would be without shifting.

The fit between model and field data is not perfect, but the general features of the data—splitting of the apparent resistivity curves in rotated coordinates, and higher xy phases—are visible in the model curves and therefore support the existence of an anisotropic layer in the middle crust. The depth of the anisotropic layer in the 1-D model (15 km) differs from that indicated by the 2-D inversions ($\approx$ 30 km). This can be due to different model resistivities and two-dimensionality above the anisotropic layer.

3.3 2-D forward modelling

Finally two-dimensional forward modelling should show if an anisotropic layer could explain the data observed along the profile. A finite element program (WANNAMAKER *et al.*, 1987) was used for the calculations. There are two ways to realize an anisotropic layer in a 2-D modelling procedure. One possibility is the use of a laminated structure where the major and minor resistivities within an anisotropic region are built up as a serial and parallel circuit of a sequence of high and low resistivities (RASMUSSEN, 1988; KELLETT *et al.*, 1992). To simulate the infinite extension of the laminated structure the minor resistivity must be assigned to the homogeneous left and right boundary regions of that layer for TE mode calculation. The major resistivity has to be assigned to these regions for TM mode calculation. Thus, the calculations for the two modes have to be performed separately.

A second method for calculating the responses is to replace the laminated region by the minor resistivity for one polarization and the major resistivity for the other. This second possibility is a special case of the first one with the assumption of infinitely narrow lamellae.

The second way of modelling anisotropy might cause problems if the over- and underlying structure has strong lateral resistivity gradients. In this case vertical currents arise in the TM

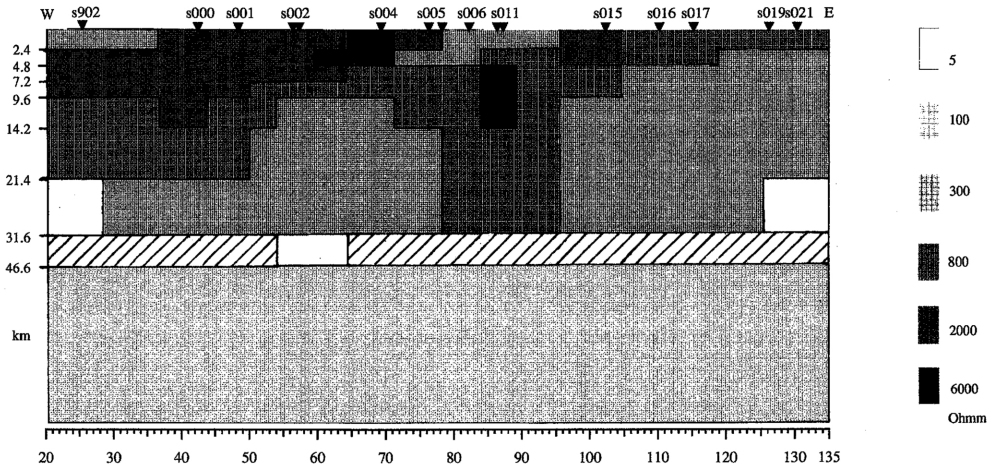

Fig. 7. The final 2-D model from forward calculations projected on the E-W striking profile. Triangles at the top show the site locations, the horizontal axis at the bottom shows the distance in kilometers. Dark grey shades indicate high resistivities, light greys indicate low resistivities. The white, hatched layer from 31.6 km to 46.6 km depth is anisotropic with a minor resistivity of 5 Ωm directed N45°E and a major resistivity of 300 Ωm perpendicular to it. The structure of the uppermost part was taken from the results of 2-D inversions, the resistivities of the anisotropic region result from 1-D forward calculations.

mode and a laminated structure would produce different results than the second technique. Because the inversion models give no evidence for strong lateral resistivity gradients above and below the anisotropic layer, the second technique is used here.

The structures of the uppermost part within the model were taken from the smooth models obtained by inverting the phases. An anisotropic layer was included at 30 km depth as suggested by the 2-D inversions (Subsection 3.1). Minor and major resistivities were taken from the estimates of the one-dimensional calculations (Subsection 3.2). The final model which was found after a few minor modifications is shown in Fig. 7. High resistivities are in dark grey shades, low resistivities in light grey. The hatched layer at 31.6 km–46.6 km depth is anisotropic with a minor resistivity of 5 Ωm and a major one of 300 Ωm.

To fit the phases—especially at longer periods, which represent the regional structure—was the main goal of the modelling process. Figure 8 shows the misfit between observed data and model responses in pseudosections for TE and TM mode. The residuals are mainly between $+6°$ and $-6°$ except for some regions where they are significantly higher. This is due to the very complex structure in the upper crust of the observed region which is not resolved in the model.

4. Conclusions

The applied decomposition scheme assumes a model which consists of a regional two-dimensional structure superimposed on by local three-dimensional regions. The results of the decomposition are the strike of the regional structure and, coupled with this strike direction, the regional phases. In this interpretation the anisotropic layer at about 30 km depths is considered to be the regional structure which influences periods longer than a few seconds. The determined strike angle of N45°E is the direction of the minimum resistivity within this layer. From this point of

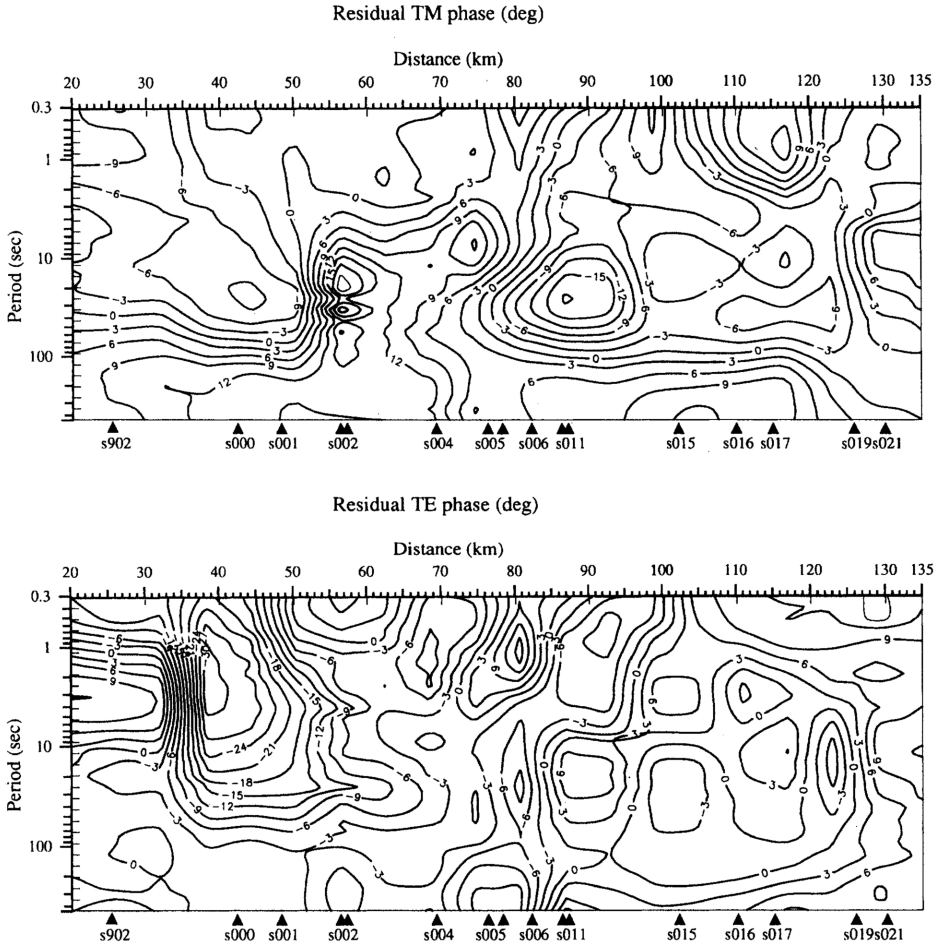

Fig. 8. Phase misfit between observed data and model data of the TE (top) and TM mode (bottom) in degrees as pseudosections along the profile. The triangles at the bottom indicate the site locations.

view the identification of the E-polarization with an electric field directed N45°E is compelling.

Disregarding the very complex structure in the upper crust there is good agreement with the model derived by JONES *et al.* (1993) which also includes an anisotropic layer at similar depth.

The increased phase-sensitive skew at 5 s period as well as the slightly varying regional strike angles along the profile give some evidence for lateral variations of the major anisotropy directions.

P. Bruton, T. M. Rasmussen and P. Zhang helped improve the original manuscript. A. Magunia produced parts of the figures. Some helpful discussions were held with V. Haak. A. G. Jones initiated the workshop and, together with D. Oldenburg, provided the field data.

LITHOPROBE Publication number 481.

APPENDIX

Table 2. Summary of regional strike angle determination at selected long periods. The first number of each column refers to the angle α, positive clockwise, calculated by Eq. 30 of BAHR (1991). The number in brackets is the "phase deviation" delta according to the modified superposition model, Eq. 2. (—) indicates that this phase deviation exceeds 5 degrees, or no solution was obtained and therefore only the conventional superposition model (Eq. 9 in BAHR (1991)) was used.

T [s] site	5.3	10.7	21.3	42.7	85.3	170.7	distortion class
s901	79. (—)	78. (—)	65. (—)	60. (—)	57. (—)	55. (—)	5/7
s902	70. (—)	64. (—)	59. (—)	56. (—)	50. (—)	45. (—)	5/7
s000	60.	60.	60.	60.	60.	60.	6
s001	45.	45.	45.	45.	45.	45.	6
s002	55.	55.	55.	55.	55.	55.	7
s003	50.	50.	50.	50.	50.	50.	7
s004	55.	55.	55.	55.	55.	55.	7
s005	55.	55.	55.	55.	55.	55.	6
s006	55. (—)	50. (—)	46. (—)	39. (—)	48. (3.9)	42. (—)	5/7
s007	50.	50.	50.	50.	50.	50.	6
s008	84. (0.3)	28. (—)	29. (—)	32. (—)	33. (—)	49. (0.1)	5/6
s009	51. (0.2)	43. (0.2)	39. (0.4)	45. (0.3)	48. (0.3)	51. (0.1)	5
s010	50. (0.0)	47. (2.9)	44. (—)	46. (3.2)	52. (0.1)	55. (1.2)	5
s011	53. (1.5)	48. (2.3)	44. (3.1)	47. (1.6)	52. (0.3)	56. (0.9)	5
s012	53. (0.3)	40. (0.6)	39. (0.8)	48. (0.4)	49. (0.3)		5
s013	74. (7.7)	60. (5.0)	56. (3.7)	54. (2.6)	57. (1.8)	61. (1.4)	5/6
s014							2
s015	36. (2.1)	36. (0.6)	27. (0.0)	42. (0.2)	49. (0.0)	53. (0.6)	5
s016	25. (1.2)	31. (0.4)	37. (1.7)	37. (1.1)	46. (0.9)	49. (0.5)	5/6
s017	33. (3.5)	41. (0.6)	39. (0.1)	45. (0.1)	48. (0.2)	52. (0.9)	5/6
s018	45. (0.5)	42. (0.3)	50. (0.1)	43. (0.4)	49. (0.3)	47. (0.3)	5
s019	49. (1.5)	40. (2.3)	39. (3.0)	47. (3.5)	48. (2.5)	51. (2.2)	5/6
s020	40. (3.2)	65. (—)	60. (—)	63. (—)	63. (—)	65. (—)	5/7
s021	61. (1.6)	69. (4.1)	61. (4.8)	66. (—)	60. (—)	60. (—)	5/7
s022	54. (—)	72. (—)	59. (—)	43. (—)	48. (—)	47. (—)	5/7
s023	61. (—)	62. (—)	66. (—)	68. (—)	64. (—)	61. (—)	5/7
s024	50. (—)	51. (—)	57. (—)	58. (—)	61. (—)	60. (5.0)	5/6

REFERENCES

BAHR, K., Interpretation of the magnetotelluric impedance tensor: regional induction and local telluric distortion, *J. Geophys.*, **62**, 119–127, 1988.

BAHR, K., Geological noise in magnetotelluric data: a classification of distortion types, *Phys. Earth Planet. Int.*, **66**, 24–38, 1991.

DEGROOT-HEDLIN, C. and S. C. CONSTABLE, Occam's inversion to generate smooth, two-dimensional models from magnetotelluric data, *Geophysics*, **55**, 1613–1624, 1990.

DEKKER, D. L. and L. M. HASTIE, Magneto-telluric impedances of an anisotropic layered Earth model, *Geophys. J. R. astr. Soc.*, **61**, 11–20, 1980.

GROOM, R. W. and R. C. BAILEY, Decomposition of the magnetotelluric impedance tensor in the presence of local three-dimensional galvanic distortion, *J. Geophys. Res.*, **94** (B2), 1913–1925, 1989.

GROOM, R. W. and K. BAHR, Corrections for near surface effects: decomposition of the magnetotelluric impedance tensor and scaling corrections for regional resistivities. A tutorial, *Surv. Geophys.*, **13**, 341–379, 1992.

JONES, A. G., The BC87 dataset: Tectonic setting, previous EM results, and recorded MT data, *J. Geomag. Geoelectr.*, this issue, 1089–1105, 1993.

JONES, A. G. and R. W. GROOM, Strike angle determination from the magnetotelluric impedance tensor in the presence of noise and local distortion: rotate at your peril!, *J. Geophys. Int.*, **113**, 524–534, 1993.

JONES, A. G., R. D. KURTZ, D. W. OLDENBURG, D. E. BOERNER, and R. ELLIS, Magnetotelluric observations along the LITHOPROBE southeastern Canadian Cordilleran transect, *Geophys. Res. Lett.*, **15**, 677–680, 1988.

JONES, A. G., R. G. GROOM, and R. D. KURTZ, Decomposition and modelling of the BC87 dataset, *J. Geomag. Geoelectr.*, this issue, 1127–1150, 1993.

KELLETT, R. L., M. MARESCHAL, and R. D. KURTZ, A model of lower crustal electrical anisotropy for the Pontiac Subprovince of the Canadian Shield, *Geophys. J. Int.*, **111**, 141–150, 1992.

RASMUSSEN, T. M., Magnetotellurics in southwestern Sweden: evidence for electrical anisotropy in the lower crust?, *J. Geophys. Res.*, **93**, 7897–7907, 1988.

TING, S. C. and G. W. HOHMANN, Integral equation modeling of three-dimensional magnetotelluric response, *Geophysics*, **46**, 182–197, 1981.

WANNAMAKER, P. E., J. A. STODT, and L. RIJO, A stable finite element solution for two-dimensional magnetotelluric modelling, *Geophys. J. R. Astr. Soc.*, **88**, 277–296, 1987.